Plasmonics
https://doi.org/10.1007/s11468-020-01324-2

# Plasmon Hybridization-Induced Ultra-broadband High Absorption from 0.4 to 1.8 Microns in Titanium Nitride Metastructures

**Shiwen Wu[1,2] · Tengfei Luo[3] · Guoping Xiong[1,2]**

Received: 14 August 2020 / Accepted: 3 November 2020


**Abstract**
Titanium nitride (TiN) metadevices as perfect absorbers are studied using finite-difference time-domain (FDTD) simulations. In this paper, we demonstrate a metastructure including a top silica ($SiO_2$) layer, two layers of TiN nano-ribbon arrays, a $SiO_2$ dielectric layer, and a TiN film to realize efficient solar energy harvesting. We theoretically optimize the geometrical parameters of each active layer to achieve high absorption rates with an average value of up to 95% within an ultra-wide band from 0.4 to 1.8 microns, covering over 93% of total energy in the solar spectrum. Our detailed analysis of the electric field enhancement indicates that such ultra-broadband high absorption in the visible/near-infrared ranges can be attributed to surface plasmon resonances, Fabry-Perot resonances, and strong plasmon hybridization between adjacent TiN nano-ribbons. Together with refractory properties of TiN and $SiO_2$, the designed metadevice may exhibit great potential in efficient solar energy harvesting applications, particularly in harsh environments.

**Keywords** Metastructures · Finite-difference time-domain method · Plasmonic hybridization · Nano-ribbon arrays · Ultra-broadband absorption

## Introduction

Clean and sustainable solar energy, which strikes the earth at a power of 120,000 TW, provides the most promising choice to overcome energy shortages in the future [1, 2]. Plasmonic materials, such as noble metal nanoparticles, have been widely investigated in the past decades [3–16] because of the strong absorption induced by localized surface plasmon resonances. Nonetheless, the solar spectrum consists of the ultraviolet, visible, and near-infrared (near-IR) regimes ranging from 0.3 to 2.5 microns, with most of the solar energy power distributed in the visible (45%) and near-IR (52%) ranges [17]. The nature of surface plasmon resonance determines their relatively narrow absorption bandwidth [6, 18, 19]. High reflectivity outside of the resonance peaks severely limits the effectiveness of plasmonic materials in solar energy harvesting applications [20]. Moreover, noble metal nanoparticles are unstable in harsh environments such as elevated temperatures due to their relatively low melting point, along with their high cost, making them non-ideal for applications such as solar thermal conversion, hot electron devices, or solar thermophotovoltaics [21, 22]. Therefore, broadband plasmonic absorbers with perfect absorption and refractory characteristics are urgently required.

Transition metal nitrides are generally considered as ideal alternative plasmonic materials of noble metals [23–26]. Among them, titanium nitride (TiN) has attracted tremendous attention because of its outstanding thermal stability (up to 2930 °C) [20, 27], unique plasmonic behavior, high carrier concentration comparable with metals [28], large loss (i.e., high solar-thermal conversion efficiency [20]), as well as excellent impedance match to air in the visible and near-IR ranges [29–31]. However, a single TiN film cannot realize broadband perfect absorption of solar energy because of its metallic characteristics in

**Electronic supplementary material** The online version of this article (https://doi.org/10.1007/s11468-020-01324-2) contains supplementary material, which is available to authorized users.

✉ Guoping Xiong
Guoping.Xiong@UTDallas.edu

[1] Department of Mechanical Engineering, The University of Texas at Dallas, Richardson, TX 75080, United States

[2] Department of Mechanical Engineering, University of Nevada, Reno, NV 89557, United States

[3] Department of Aerospace and Mechanical Engineering, University of Notre Dame, Notre Dame, IN 46556, United States

Published online: 06 January 2021

the wavelength (denoted as $\lambda$) range of $\lambda > 0.55$ μm [20]. Although efforts have been made to design various structures to broaden the absorption of TiN, the absorption of such absorbers is still limited to the visible range [20, 32–37] or a relatively narrow part in the near-IR range (i.e., $\lambda < 1.2$ μm) [38, 39]. Therefore, new designs of TiN metastructures with broader absorption bands that encompass the majority of solar power are highly desired for efficient solar energy harvesting.

Here, we propose a uniquely designed device based on dielectric materials and TiN metastructures as ultra-broadband high-efficiency absorbers in the visible and majority of the near-IR range (covering over 93% of the total energy in the solar spectrum). The metadevice consists of a top $SiO_2$ layer, two layers of TiN nano-ribbon arrays, a $SiO_2$ dielectric layer, and a TiN film. High absorption rates with an average value of up to 95% from 0.4 to 1.8 microns can be achieved by optimizing the geometric parameters of each layer. Detailed analysis of the electric field distribution within the TiN metastructures indicates that the ultra-broadband perfect absorption results from a combination of surface plasmon resonances of TiN, effect of the top $SiO_2$ layer, Fabry-Perot resonances by the TiN-$SiO_2$-TiN sandwich structure, and surface plasmon hybridization between adjacent TiN nano-ribbons.

## Structure and Computational Method

The schematic diagram of the TiN absorber is shown in Fig. 1. Figure 1a shows a global view of the designed metastructure, where silicon (Si) is employed as a physical support without any optical absorption [33, 38]. The TiN-based metadevice consists of a top $SiO_2$ layer, two spatially crossed layers of TiN nano-ribbon arrays embedded in a $SiO_2$ dielectric layer, and a TiN film. Figure 1b presents the x-z side view of the metadevice, where $p$ represents a single period of TiN nano-ribbon arrays and $w$ represents the width of TiN nano-ribbons. The y-z side view of the metadevice is shown in Fig. 1c; the thickness of top $SiO_2$ layer, thickness of TiN nano-ribbon arrays, gap between two TiN nano-ribbon layers, gap between the bottom TiN nano-ribbon layer and TiN film, and thickness of TiN film are denoted as $d_1$, $d_2$, $d_3$, $d_4$, and $d_5$, respectively.

We use commercial finite-difference time-domain (FDTD) software (Lumerical 2020a) with a three-dimensional (3D)

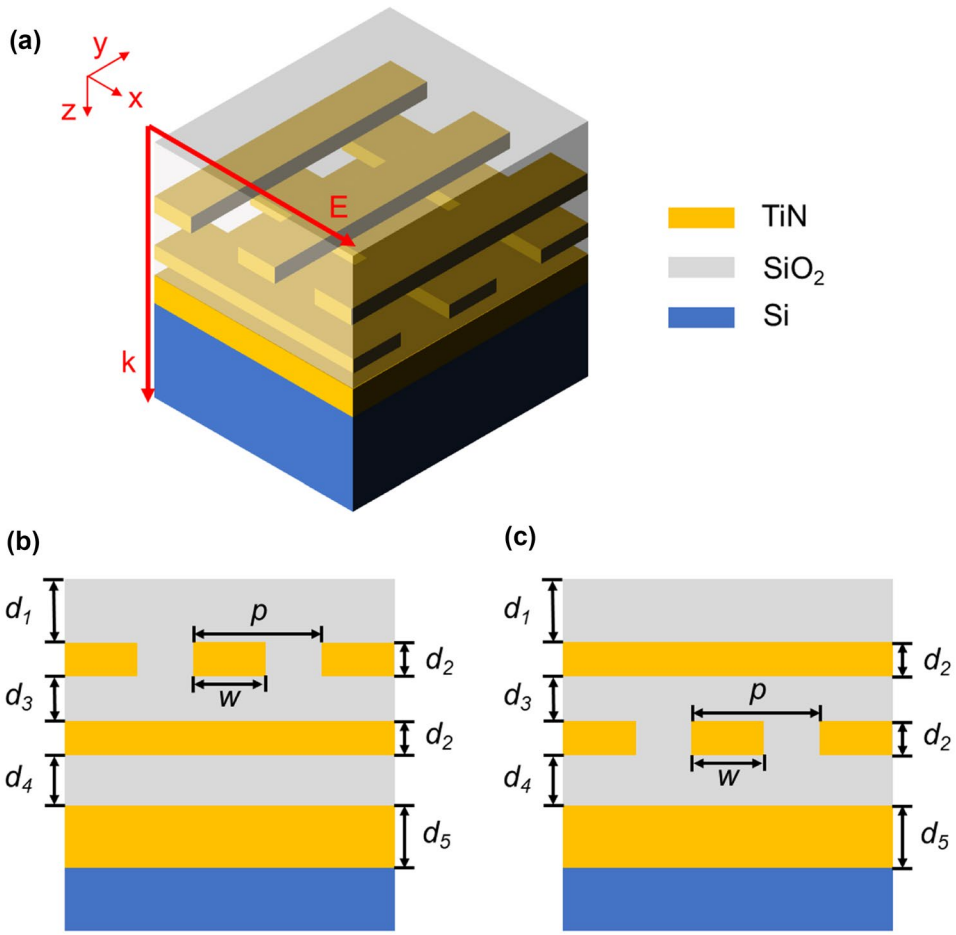


**Fig. 1** Schematic diagram of the TiN ultra-broadband perfect absorber. (**a**) Global view. (**b**) x-z side view. (**c**) y-z side view. The width of a single TiN nano-ribbon is denoted as $w$, and $p$ represents the period of TiN nano-ribbon arrays in both $x$ and $y$ directions. The thickness of top $SiO_2$ layer, thickness of TiN nano-ribbon arrays, gap between two TiN nano-ribbon layers, gap between the bottom TiN nano-ribbon layer and TiN film, and thickness of TiN film are denoted as $d_1$, $d_2$, $d_3$, $d_4$ and $d_5$, respectively

model constructed in the FDTD solver to simulate the interaction between incident light and the TiN metadevice. Periodic boundary conditions were employed both in the $x$ and $y$ directions to mimic the periodic structure of TiN nano-ribbon arrays, and perfect matching layer (PML) boundary condition was used in the $z$ direction. The optical constants of TiN were obtained from experimental data from prior work [40], and $SiO_2$ was set to have a refractive index of 1.45 [33, 38]. A plane wave was incident to the structural plane normally with the electric field along $x$ axis, as shown in Fig. 1a. We define transverse-electric (TE) polarization as polarization along $x$ axis and transverse-magnetic (TM) polarization as polarization along $y$ axis. The reflectance ($R$) and transmittance ($T$) spectra were monitored by power monitors placed 1 μm above and under the TiN metadevice. Calculations of spectra with different spacings between the TiN structure and the power monitors were performed to ensure the reliability of results (Supplementary Fig. S1). The absorbance ($A$) spectrum can be calculated from the corresponding reflectance and transmittance as $A = 1 - R - T$. We calculate the mathematically weighted average value of each absorption curves (denoted as $a$) over the spectrum range of 0.4 to 1.8 microns to evaluate the solar energy absorption capability. An average value of $a$ in TE and TM polarizations (denoted as $\bar{a}$) is calculated to represent the total absorption rate of the TiN metadevice under practical solar illumination. In all simulations, mesh sizes of 5 nm in the $x$ and $y$ directions and 2 nm in the $z$ direction were employed.

## Results and Discussion

To characterize the light absorption capability, we calculate the absorption spectra of the TiN absorber in TE and TM polarizations under a normal incidence of light illumination with a wavelength ranging from 0.4 to 1.8 microns. As shown in Fig. 2, the metadevice exhibits ultra-broadband perfect absorption from 0.4 to 1.8 microns with $a$ of 96.5% in TE polarization and 92.5% in TM polarization (i.e., with an average absorption rate $\bar{a}$ close to 95%), covering 93% of the total energy in the solar spectrum [6], significantly higher than the reported values in prior work (e.g., approx. 80% or lower when $\lambda < 1.2$ μm) [38]. The outstanding light absorption of the metadevice within such a broadband in the solar spectrum indicates its great potential in high-performance solar energy harvesting applications, particularly in harsh environments (e.g., elevated temperatures). Furthermore, compared with devices based on metal (e.g., gold, copper, and aluminum) nano-ribbon arrays, the metadevice based on TiN nano-ribbon arrays exhibits substantially better absorption capability, particularly in the near-IR region (see Supplementary Fig. S2). The optical constants of gold, copper, and aluminum are obtained from CRC Handbook

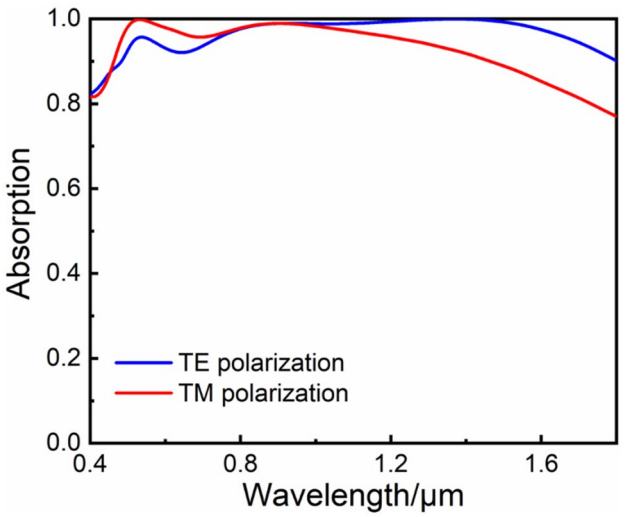


**Fig. 2** Absorption spectra of the TiN absorber under a normal incidence of light in TE and TM polarizations, when $w$ = 165 nm, $p$ = 400 nm, $d_1$ = 89 nm, $d_2$ = 16 nm, $d_3$ = 49 nm, $d_4$ = 70 nm, and $d_5$ = 150 nm. The parameters are optimized by elaborate calculations to achieve ultra-broadband high absorption

[41]. We note that the absorption spectra in both TE and TM polarizations consist of several noticeable resonance peaks around 0.5 μm, 0.9 μm, and 1.3 μm, which we will discuss subsequently to elucidate the underlying mechanisms of such strong absorption characteristics of the metadevice.

The size of the absorber is one of the key parameters determining light absorption and electromagnetic fields [33]. Hence, we investigate the influence of the TiN nano-ribbon width ($w$) (period $p$ is fixed at 400 nm) on the absorption spectra of TiN absorbers. To simplify the optimization, we set the width of TiN nano-ribbons in the two embedded layers the same value. Figures 3a and b show the absorption spectra from a wavelength of 0.4 to 1.8 microns as a function of $w$ in TE and TM polarizations, respectively. As a representative example, we analyzed the absorption rate in TE polarization at several typical widths (Fig. 3c). When $w$ changes from 0 to 400 nm, the absorption rate for both TE and TM polarizations increases first and weakens subsequently in the near-IR range. This interesting phenomenon may be explained from plasmonic hybridization within the patterned TiN nano-ribbons. Plasmonic hybridization between modes in two adjacent edges is known to result in a pair of new hybrid modes [42], and the plasmon wave vector of nano-ribbon arrays approximately obeys the relation $q \sim \frac{\pi}{w}$, which has been corroborated in many other two-dimensional plasmonic materials (e.g., graphene [43] and black phosphorus [44]). Therefore, as the width of TiN nano-ribbons increases, the resonant peaks, particularly those in the near-IR range, shift to longer wavelengths in TE polarization, as indicated by the yellow dashed arrow in Fig. 3c. The superposition of these resonant peaks within the visible and part of the near-IR ranges

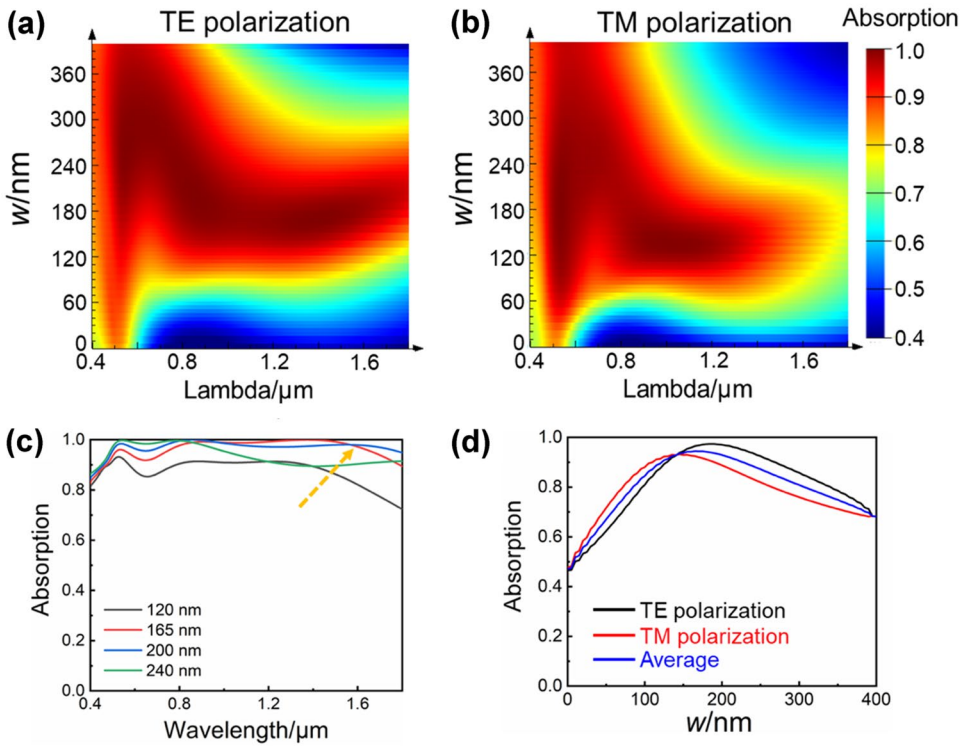


**Fig. 3** Absorption spectra as a function of the width of TiN nano-ribbons ($w$) in the selected solar spectrum: when $w$ changes from 0 to 400 nm in (**a**) TE and (**b**) TM polarizations with the same color bar. (**c**) Absorption spectra at several typical widths in TE polarization. (**d**) Calculated absorption rates as a function of the width of TiN nano-ribbons. Other parameters are fixed as $p = 400$ nm, $d_1 = 89$ nm, $d_2 = 16$ nm, $d_3 = 49$ nm, $d_4 = 70$ nm, and $d_5 = 150$ nm

leads to high absorption rates. Note that the absorption rate is relatively low with a small $w$, which can be attributed to a low filling factor of TiN nano-ribbons and weaker plasmon hybridization between adjacent nano-ribbons. We further calculate the absorption rates $a$ in TE and TM polarizations and their averaged value $\bar{a}$ at different widths ranging from 0 to 400 nm (Fig. 3d) to determine the optimal width to achieve maximum

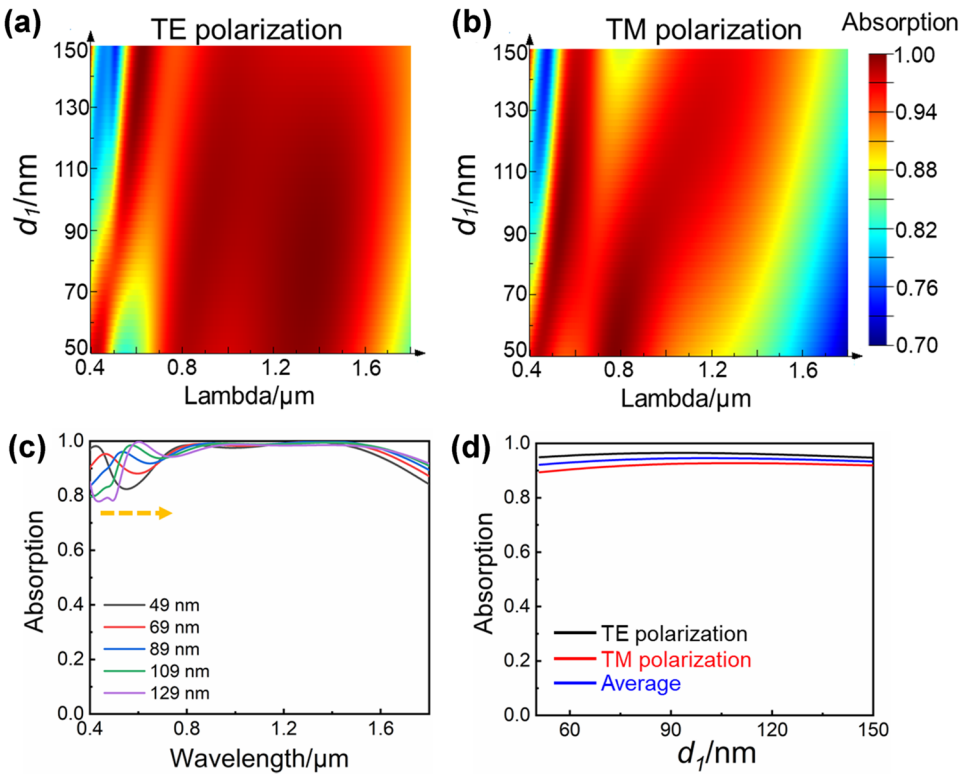


**Fig. 4** Absorption spectra as a function of the thickness ($d_1$) of top $SiO_2$ layer in the selected solar spectrum: when $d_1$ changes from 49 to 151 nm in (**a**) TE and (**b**) TM polarization with the same color bar. (**c**) Absorption spectra at several typical thicknesses in TE polarization. (**d**) Calculated absorption rates as a function of $d_1$. Other parameters are fixed as $w = 165$ nm, $p = 400$ nm, $d_2 = 16$ nm, $d_3 = 49$ nm, $d_4 = 70$ nm, and $d_5 = 150$ nm

absorption. As shown in Fig. 3d, the optimized $\bar{a}$ is achieved at $w = 165$ nm while keeping other parameters fixed.

The top dielectric layer can enhance the absorption of nano-structured absorbers by reducing structural reflection, while excessively thick top dielectric layers influence surface plasmon resonances in the TiN structure [20, 45]. We investigate the influence of the thickness of top $SiO_2$ layer ($d_1$) on absorption properties of the TiN metadevice. Figures 4a and 4 display the absorption spectra in TE and TM polarizations, respectively, as the thickness of the top $SiO_2$ layer varies from 49 to 151 nm. As shown in Fig. 4a and b, the thickness of top $SiO_2$ layer apparently affects the absorption spectra, particularly in the visible range and part ($\lambda > 1.6$ μm) of the near-IR range, by shifting some resonant peaks. The thickness of the top dielectric layer may affect surface plasmon resonances between TiN nano-ribbons and thus effectively control the plasmonic resonance peaks of the TiN absorber. We select the spectra at several typical thicknesses to facilitate revealing the influence of the top dielectric layer on the absorption of the metadevice in TE polarization, as shown in Fig. 4c. Increasing the thickness of the top dielectric layer results in a red shift of the resonant peaks in the visible range (indicated by the yellow dashed arrow in Fig. 4c). An optimized top dielectric layer thickness can modulate the peak resonances to achieve an ultra-broadband absorption [38].

Figure 4d shows the calculated absorption rates in TE and TM polarizations, along with the average absorption rate ($\bar{a}$) of the two polarizations at different thicknesses (ranging from 49 to 151 nm). The results show that the optimized average absorption rate,$\bar{a}$, can be achieved at a top $SiO_2$ layer thickness of 89 nm while keeping other parameters fixed.

We further study the effect of TiN nano-ribbon thickness ($d_2$) on the absorption rate of the metadevice. Absorption spectra for TE and TM polarizations with $d_2$ ranging from 6 to 40 nm are shown in Fig. 5a and b, respectively, in which the absorption capability is evaluated by changing $d_2$ while fixing other parameters. When the thickness of TiN nano-ribbon arrays is excessively thin, interaction between light and TiN is insufficient, leading to a relatively low absorption; on the other hand, increasing the thickness of TiN nano-ribbon arrays to over 16 nm results in poor matching with free space impedance and thus cannot excite strong surface plasmon resonances [33], leading to deterioration in light absorption at wavelengths in the near-IR range (from 0.8 to 1.8 microns), as indicated by the yellow dashed arrows in Fig. 5c. Moreover, compared with the modes in the visible range, it appears that those in the near-IR range are more sensitive to the variation of TiN nano-ribbon thickness. The total averaged light absorption rate ($\bar{a}$) of the TiN metadevice in TE and TM polarizations (Fig. 5d) shows that the

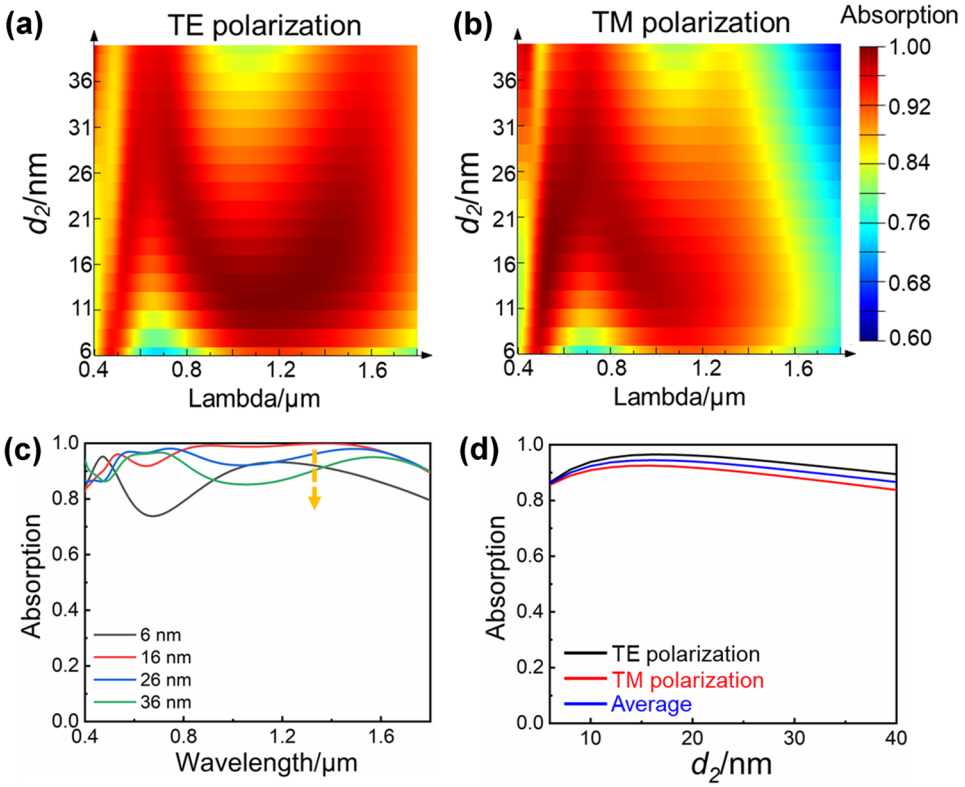


**Fig. 5** Absorption spectra as a function of the thickness of TiN nano-ribbon arrays ($d_2$) in the selected solar spectrum: when $d_2$ changes from 6 to 40 nm in (**a**) TE and (**b**) TM polarizations with the same color bar. (**c**) Absorption spectra at several typical thicknesses in TE polarization. (**d**) Calculated absorption rates as a function of $d_2$. Other parameters are fixed as $w = 165$ nm, $p = 400$ nm, $d_1 = 89$ nm, $d_3 = 49$ nm, $d_4 = 70$ nm, and $d_5 = 150$ nm

optimized $\bar{a}$ can be achieved at $d_2 = 16$ nm while keeping other parameters fixed.

The thickness of the dielectric material ($d_3$) between two TiN nano-ribbon layers and the thickness of the dielectric material ($d_4$) between the bottom TiN nano-ribbon layer and TiN film also affect the optical properties of the metadevice. We thus investigate the influence of $d_3$ and $d_4$ on the absorption rate of the metadevice while keeping other parameters fixed as $w = 165$ nm, $p = 400$ nm, $d_1 = 89$ nm, $d_2 = 16$ nm, and $d_5 = 150$ nm, the results of which are shown in Figs. 6 and 7, respectively. Figures 6a and b display the absorption spectra of the metadevice in TE and TM polarizations, respectively, with $d_3$ ranging from 0 to 85 nm. Figure 6c shows the absorption spectra of the metadevice in TE polarization at several typical $d_3$ values. From Fig. 6a-c, one can see that varying $d_3$ results in the changes of peak position and intensity both in TE and TM polarizations. As $d_3$ increases from 9 to 69 nm, the peak location in the visible range undergoes a red shift, changing from approx. 0.45 to 0.5 μm, with a slightly decreased peak intensity, while the two peaks located in the near-infrared range (e.g., 0.9 and 1.1 μm when $d_3 = 9$ nm) gradually separate from each other with high peak intensities (> 95%), as indicated by the yellow dashed arrows in Fig. 6c. The mathematically calculated absorption rates ($a$) in TE and TM polarizations, along with the averaged rate $\bar{a}$, are shown in Fig. 6d, in which one can see that the absorption rate, $a$, in TE polarization increases first and then decreases after $d_3$ reaches an optimal value. On the other hand, the absorption rate in TM polarization increases steadily with increasing $d_3$. From the $\bar{a}$ curves in Fig. 6d, the optimized average absorption rate is achieved at $d_3 = 49$ nm. Figures 7a and b display the absorption spectra of the metadevice in TE and TM polarizations, respectively, with $d_4$ ranging from 30 to 110 nm. Figure 7c shows the absorption spectra of the metadevice in TE polarization at several typical $d_4$ values. Similar trends are observed in Fig. 7a-c as $d_4$ increases from 30 to 110 nm in TE polarization. Figure 7d shows that the absorption rates, $a$, in both TE and TM polarizations increase first and then decrease as $d_4$ increases. By calculating the average absorption rate, $\bar{a}$, in TE and TM polarizations, one can see that an optimal $\bar{a}$ of the metadevice occurs at $d_4 = 70$ nm while fixing other parameters.

The excellent optical properties of the metadevice can be attributed to the unique structural design and working mechanisms. The double-layer TiN nano-ribbon structure and TiN film acting as two mirrors, together with the sandwiched $SiO_2$ dielectric layer, form a Fabry-Perot cavity, enhancing the interaction between light and the TiN absorber. Parameters such as nanostructure size, separation, and pattern design can significantly influence the effect of Fabry-Perot interference [44, 46]. $SiO_2$ dielectric layer with an optimal

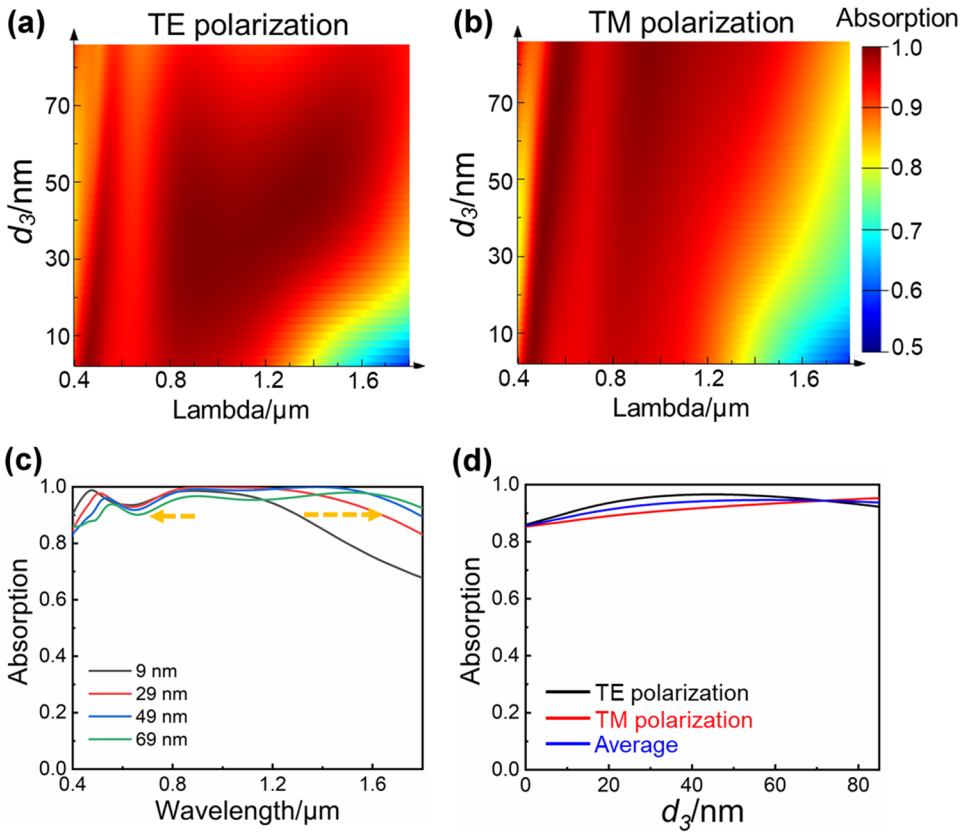


**Fig. 6** Absorption spectra as a function of the thickness of the dielectric material ($d_3$) between two TiN nano-ribbon layers in the selected solar spectrum: when $d_3$ changes from 0 to 85 nm in (**a**) TE and (**b**) TM polarizations with the same color bar. (**c**) Absorption spectra at several typical thicknesses in TE polarization. (**d**) Calculated absorption rates as a function of $d_3$. Other parameters are fixed as $w = 165$ nm, $p = 400$ nm, $d_1 = 89$ nm, $d_2 = 16$ nm, $d_4 = 70$ nm, and $d_5 = 150$ nm

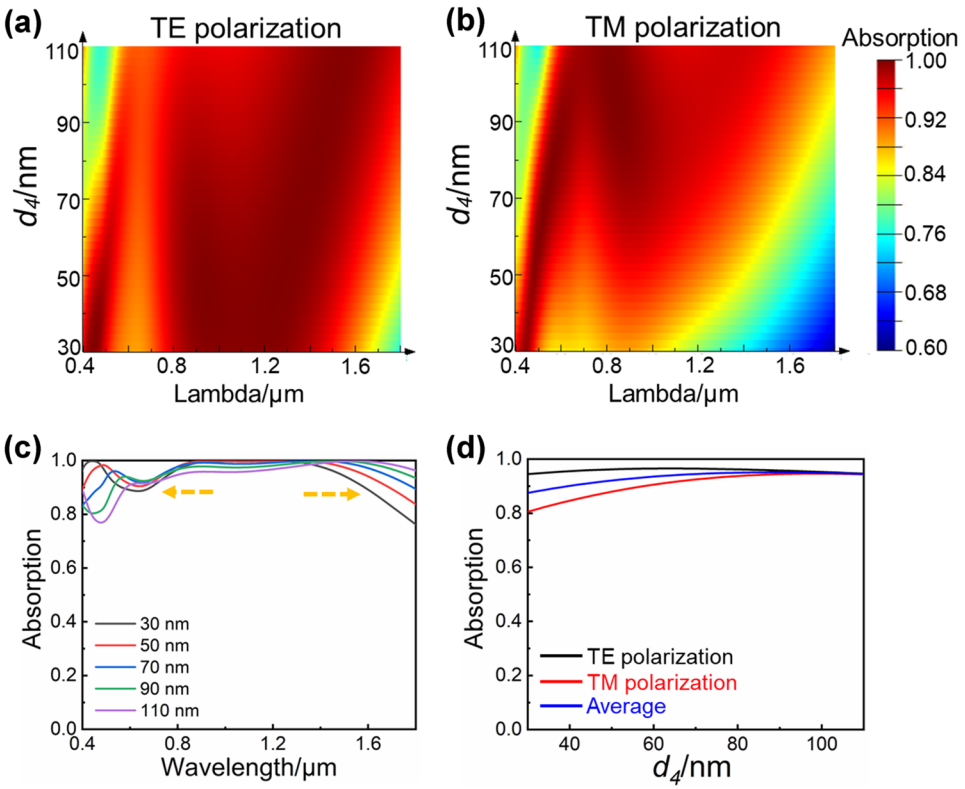


**Fig. 7** Absorption spectra as a function of the thickness of the dielectric material ($d_4$) between the bottom TiN nano-ribbon layer and TiN film in the selected solar spectrum: when $d_4$ changes from 30 to 110 nm in (**a**) TE and (**b**) TM polarizations with the same color bar. (**c**) Absorption spectra at several typical thicknesses in TE polarization. (**d**) Calculated absorption rates as a function of $d_4$. Other parameters are fixed as $w = 165$ nm, $p = 400$ nm, $d_1 = 89$ nm, $d_2 = 16$ nm, $d_3 = 49$ nm, and $d_5 = 150$ nm

thickness between two plasmonic TiN nano-ribbon layers can excite strong surface plasmon resonances by matching free space impedance, while an excessively thin or thick dielectric layer may result in a reduction of absorption rate. Such an absorber with a unique structural design can be regarded as a combination of two Fabry-Perot cavities, with one formed by the top TiN nano-ribbon layer and the TiN film with a gap of $d_3 + d_4$ (denoted as cavity T), and the other one formed by the bottom TiN nano-ribbon layer and the TiN film with a gap of $d_4$ (denoted as cavity B). When illuminated by the incident light, the nano-ribbon array layer with ribbons perpendicular to the polarization direction dominates the interaction with the incident light. Therefore, the light absorption peaks in TE polarization are primarily attributed to strong interactions of the top TiN nano-ribbon array layer with light, while the ones in TM polarization arise from the interaction of the bottom array layer with light. When increasing $d_3$ at a fixed $d_4$, the gap $(d_3 + d_4)$ in cavity T increases accordingly. As a result, as we increase the value of $d_3$, the absorption in TE polarization increases first until the gap in cavity T reaches an optimal value, after which the absorption decreases gradually. When illuminated by TM-polarized light, the bottom TiN nano-ribbon array layer becomes active, and thus cavity B dominates the interaction with the incident light. The gap $(d_4)$ in cavity B remains fixed as $d_3$ increases. However, the absorption in TM polarization keeps increasing when $d_3$ increases. This may be attributed to the reducing interference of the top TiN nano-ribbon layer on cavity B as $d_3$ increases. On the other hand, while changing the value of $d_4$ with $d_3$ fixed, gaps in both Fabry-Perot cavities change. Therefore, absorption rates in both TE and TM polarizations increase first and then decrease after $d_4$ reaches an optimized value.

Investigating the optical properties of such TiN absorbers under various light polarization angles is essential to their practical solar energy harvesting applications. We study the absorption capability of the TiN absorbers by varying the light polarization angle from 0° to 90°. The simulations can cover all polarization angles of solar light because the structure of as-designed TiN metadevices is both x- and y-symmetric. Figure 8a shows the absorption spectra of the metadevice in different polarization directions, and Fig. 8b provides the mathematically weighted average absorption rate, $a$, in the selected spectrum at each polarization angle. As shown in Fig. 8a and b, such a TiN optical metadevice with a uniquely designed structure exhibits high absorption (close to 95%) throughout all polarization angles, which is in sharp contrast with absorbers based on single-layer TiN nano-ribbon arrays (Supplementary Fig. S3), demonstrating their great potential in practical solar energy harvesting applications.

To reveal the physical origin of such ultra-broadband high absorption in the TiN metadevice, we calculate the electric field distribution at various resonant wavelengths. Figure 9a

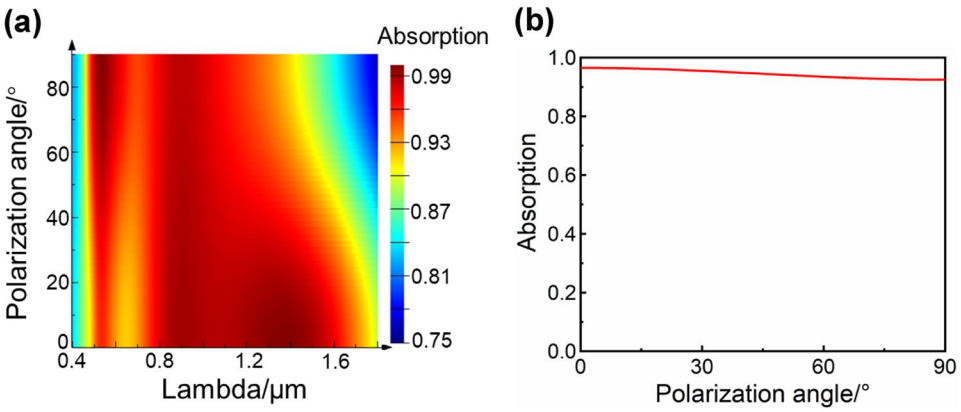


**Fig. 8(a)** Absorption spectra as a function of the polarization angle of incident light in the selected solar spectrum. (**b**) Average absorption rate, $a$, as a function of the polarization angle of incident light. Other parameters are fixed as $w = 165$ nm, $p = 400$ nm, $d_1 = 89$ nm, $d_2 = 16$ nm, $d_3 = 49$ nm, $d_4 = 70$ nm, and $d_5 = 150$ nm

shows the schematic diagram of the x-z cross section of a unit cell, and Fig. 9b-d displays the electric field distributions at the x-z cross section in TE polarization at wavelengths of 0.535 μm, 0.911 μm, and 1.376 μm, respectively. The magnitude of the electric field enhancement at the x-z cross section in TE polarization is substantially higher than that at the y-z cross section in TE polarization (Supplementary Fig. S4), confirming that the TiN nano-ribbon layer with ribbons perpendicular to the light polarization direction dominates the interactions with incident light. At a wavelength of 0.535 μm (Fig. 9b), the electric field is mainly distributed in the space between the top TiN nano-ribbon layer and the TiN film, which is caused by Fabry-Perot resonances induced in the TiN-dielectric-TiN structure. In the Fabry-Perot cavity structure, the top TiN nano-ribbon layer and TiN film act as mirrors to reflect light between them, leading to electric field localization [44, 47]. Notably, apparent electric field 'hot spots' at the edges of TiN nano-ribbons at $\lambda = 0.911$ μm and 1.376 μm are observed (Fig. 9c and d), illustrating strong plasmon hybridization between adjacent TiN nano-ribbons, which can also be verified by the electric vector field distribution in Supplementary Fig. S5. The hybridization between two adjacent ribbon edges leads to a split of single edge mode into two new modes. Depending on antisymmetric or symmetric plasmon hybridization, the frequencies of the generated new hybrid modes are usually higher or lower than that of the intrinsic edge mode [42]. Such a unique plasmon hybridization mechanism results in an ultra-high light absorption rate (99.9%) at $\lambda = 1.376$ μm and thus extends the upper wavelength limit of perfect absorption of the TiN metadevice to over 1.8 μm, achieving an ultra-broadband perfect solar absorption (covering 93% of the total energy in the solar spectrum), superior to those reported in prior work (i.e., $\lambda < 1.2$ μm) [20, 22, 32–38]. A comparison of the absorption performance of our proposed TiN metadevice and previous TiN structures is shown in Supplementary Table S1. Moreover, the intensity and location of these absorption peaks are quite sensitive to the configuration parameters (e.g., thickness, width) of each active layer within the metadevice. This allows us to tune resonant peaks by controlling these parameters of the active layers and thus effectively optimize the absorption performance of the TiN metadevice.

When the polarization mode of incident light changes from TE to TM, the active layer that dominates the interaction with light changes to the bottom TiN nano-ribbon layer (Fig. 10 and Supplementary Fig. S6). Figure 10a shows the schematic diagram of the y-z cross section of a unit cell. Figures 10b-d display the electric field strength distributions at the y-z cross section in TM polarization at wavelengths

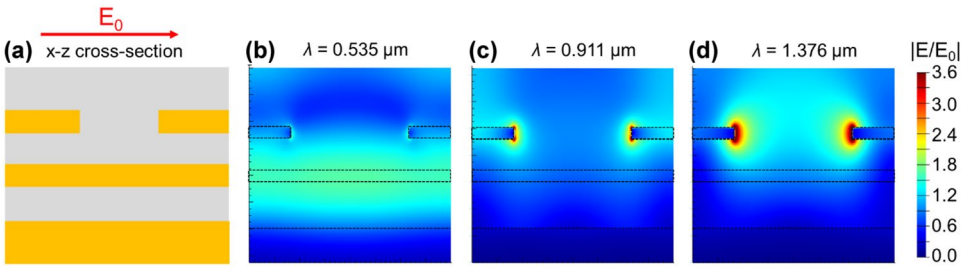


**Fig. 9(a)** Schematic diagram of the x-z cross section of a unit cell. The magnitude and distribution of the electric field $|E/E_0|$ at the x-z cross section of a unit cell illuminated in TE polarization at (**b**) $\lambda = 0.535$ μm, (**c**) $\lambda = 0.911$ μm, and (**d**) $\lambda = 1.376$ μm with the same color bar. The parameters of the metadevice: $w = 165$ nm, $p = 400$ nm, $d_1 = 89$ nm, $d_2 = 16$ nm, $d_3 = 49$ nm, $d_4 = 70$ nm, and $d_5 = 150$ nm

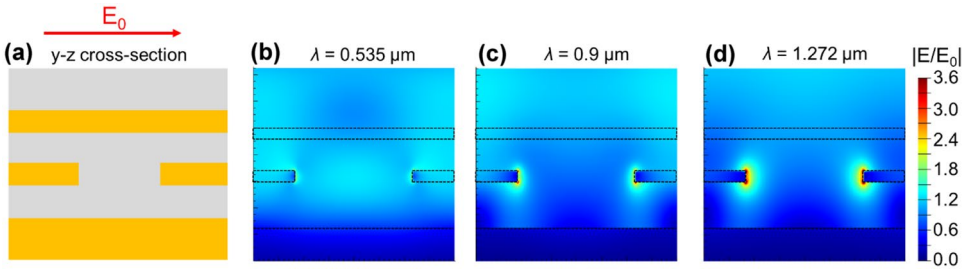


**Fig. 10(a)** Schematic diagram of the y-z cross section of a unit cell. The magnitude and distribution of the electric field $|E/E_0|$ at the y-z cross section of a unit cell illuminated in TM polarization at (**b**)$\lambda = 0.535$ μm, (**c**) $\lambda = 0.9$ μm, and (**d**) $\lambda = 1.272$ μm with the same color bar. The parameters of the metadevice: $w = 165$ nm, $p = 400$ nm, $d_1 = 89$ nm, $d_2 = 16$ nm, $d_3 = 49$ nm, $d_4 = 70$ nm, and $d_5 = 150$ nm

of 0.535 μm, 0.9 μm, and 1.272 μm, respectively. Similar to the electric field distribution in TE polarization, the resonant peak located at 0.535 μm is mainly attributed to the Fabry-Perot resonances in the cavity formed by the bottom TiN nano-ribbon layer and TiN film. At wavelengths of 0.9 μm and 1.272 μm (Fig. 10c and d), apparent 'hot spots' appear at the edges of TiN nano-ribbons in the bottom layer. These 'hot spots' are caused by plasmon hybridization between adjacent TiN nano-ribbons, which can also be verified by the electric vector field distribution in Supplementary Fig. S7. Therefore, the ultra-broadband perfect absorption property of the uniquely designed TiN metastructure in the solar spectrum can be attributed to a combination of surface plasmon resonances, Fabry-Perot resonances and strong plasmon hybridization between adjacent TiN nano-ribbons. The unique double-layer TiN nano-ribbon array structure provides high broadband absorption over all polarization angles, which is essential to practical solar energy harvesting applications. In addition, experimental preparation of such metadevices is feasible. The TiN film can be fabricated in large areas by plasma-assisted chemical vapor deposition (PECVD) [48], while the TiN nano-ribbon arrays can be fabricated by electron beam lithography. We will verify the proposed structural design by experiment and report separately upon further investigation for the future work.

## Conclusion

In summary, we have proposed and designed a TiN metastructure as ultra-broadband perfect absorbers, consisting of a top $SiO_2$ layer, two layers of TiN nano-ribbon arrays, a $SiO_2$ dielectric layer, and a TiN film with a total thickness of 390 nm. The metadevice achieves an average absorption rate of up to 95% from 0.4 to 1.8 microns, which covers over 93% of solar energy in the solar spectrum, exhibiting great potential for solar energy harvesting applications. Moreover, such a metadevice is constructed by refractory TiN plasmonic material and $SiO_2$ which are stable at high temperatures up to 1650 °C, providing their possible applications in high-temperature or harsh environments (e.g., solar thermophotovoltaics). Simulation results reveal that such ultra-broadband perfect absorption is attributed to a combination of surface plasmon resonances, Fabry-Perot resonances and strong plasmon hybridization between adjacent TiN nano-ribbons. In addition, the unique double-layer TiN nano-ribbon structure ensures the high absorption capability throughout all polarization angles. The designed TiN metadevice also shows great promise in solar energy harvesting applications such as solar vapor generation, solar cell, and photocatalysis.

**Acknowledgments** The authors thank Dr. Eungkyu Lee for the help and discussion involved in this work.

**Authors' Contributions** All authors contributed to the study conception and design. Under the supervision of G.X., S.W. performed simulations and theoretical calculations. G.X., S.W., and T.L. analyzed the data and interpreted the results. S.W. wrote the first draft of the manuscript, and all authors contributed to the writing of the manuscript and approved the final manuscript.

**Funding** The authors received the financial support from University of Nevada, Reno startup fund, The University of Texas at Dallas startup fund, and National Science Foundation (Grant No. CBET-1937949 and CBET-1937923).

**Data Availability** The datasets analyzed during the current study are available from the corresponding author on reasonable request.

## Compliance with Ethical Standards

**Competing Interest** The authors declare that they have no competing interest.

**Ethical Approval** Not applicable.

**Consent to Participate** Not applicable.

**Consent to Publish** Not applicable.

## References


1. Blankenship RE, Tiede DM, Barber J, Brudvig GW, Fleming G, Ghirardi M, Gunner MR, Junge W, Kramer DM, Melis A, Moore TA, Moser CC, Nocera DG, Nozik AJ, Ort DR, Parson WW, Prince RC, Sayre RT (2011) Comparing photosynthetic and photovoltaic efficiencies and recognizing the potential for improvement. Science 332(6031):805–809
2. Wu S, Xiong G, Yang H, Gong B, Tian Y, Xu C, Wang Y, Fisher T, Yan J, Cen K, Luo T, Tu X, Bo Z, Ostrikov K (2019) Multifunctional solar waterways: Plasma-enabled self-cleaning nanoarchitectures for energy-efficient desalination. Advanced Energy Materials 9(30):1901286
3. Bhardwaj S, Pathak NK, Ji A, Uma R, Sharma RP (2017) Tunable properties of surface plasmon resonance of metal nanospheroid: graphene plasmon interaction. Plasmonics 12(1):193–201
4. Lu R, Xu L, Ge Z, Li R, Xu J, Yu L, Chen K (2016) Improved efficiency of silicon nanoholes/gold nanoparticles/organic hybrid solar cells via localized surface plasmon resonance. Nanoscale Res Lett 11(1):160
5. Manai L, Dridi Rezgui B, Benabderrahmane Zaghouani R, Barakel D, Torchio P, Palais O, Bessais B (2016) Tuning of light trapping and surface plasmon resonance in silver nanoparticles/C-Si structures for solar cells. Plasmonics 11(5):1273–1277
6. Pang Y, Zhang J, Ma R, Qu Z, Lee E, Luo T (2020) Solar–thermal water evaporation: a review. ACS Energy Letters 5(2):437–456
7. Lee E, Huang D, Luo T (2020) Ballistic supercavitating nanoparticles driven by single Gaussian beam optical pushing and pulling forces. Nature Communications 11(1):2404
8. Wang BX, Zhai X, Wang G-Z, Huang W-Q, Wang L-L (2015) A novel dual-band terahertz metamaterial absorber for a sensor application. J Appl Phys 117(1):014504
9. Wang BX, Wang G, Wang L, Zhai X (2016) Design of a five-band terahertz absorber based on three nested split-ring resonators. IEEE Photonics Technology Letters 28(3):307–310
10. Wang BX, Wang G-Z, Sang T (2016) Simple design of novel triple-band terahertz metamaterial absorber for sensing application. J Phys D Appl Phys 49(16):165307
11. Wang BX, Wang G-Z, Wang L-L (2016) Design of a novel dual-band terahertz metamaterial absorber. Plasmonics 11(2):523–530
12. Wang BX (2017) Quad-band terahertz metamaterial absorber based on the combining of the dipole and quadrupole resonances of two SRRs. IEEE Journal of Selected Topics in Quantum Electronics 23(4):1–7
13. Wang BX, Wang G-Z, Sang T, Wang LL (2017) Six-band terahertz metamaterial absorber based on the combination of multiple-order responses of metallic patches in a dual-layer stacked resonance structure. Scientific Reports 7(1):41373
14. Wang BX, Tang C, Niu Q, He Y, Chen T (2019) Design of narrow discrete distances of dual-/triple-band terahertz metamaterial absorbers. Nanoscale Res Lett 14(1):64
15. Wang BX, He Y, Lou P, Huang WQ, Pi F (2020) Penta-band terahertz light absorber using five localized resonance responses of three patterned resonators. Results in Physics 16:102930
16. Wang BX, He Y, Lou P, Xing W (2020) Design of a dual-band terahertz metamaterial absorber using two identical square patches for sensing application. Nanoscale Advances 2(2):763–769
17. Gao M, Zhu L, Peh CK, Ho GW (2019) Solar absorber material and system designs for photothermal water vaporization towards clean water and energy production. Energy & Environmental Science 12(3):841–864
18. Maier SA (2007) Plasmonics: Fundamentals and applications. In. p 245
19. Wang BX, Tang C, Niu Q, He Y, Chen R (2019) A broadband terahertz metamaterial absorber enabled by the simple design of a rectangular-shaped resonator with an elongated slot. Nanoscale Advances 1(9):3621–3625
20. Li W, Guler U, Kinsey N, Naik GV, Boltasseva A, Guan J, Shalaev VM, Kildishev AV (2014) Refractory plasmonics with titanium nitride: broadband metamaterial absorber. Advanced Materials 26(47):7959–7965
21. Chernyshev AP (2009) Effect of nanoparticle size on the onset temperature of surface melting. Materials Letters 63(17):1525–1527
22. Patsalas P, Kalfagiannis N, Kassavetis S (2015) Optical properties and plasmonic performance of titanium nitride. Materials 8(6):3128–3154
23. Naik GV, Kim J, Boltasseva A (2011) Oxides and nitrides as alternative plasmonic materials in the optical range [Invited]. Opt Mater Express 1(6):1090–1099
24. Naik GV, Shalaev VM, Boltasseva A (2013) Alternative plasmonic materials: beyond gold and silver. Advanced Materials 25(24):3264–3294
25. Guler U, Shalaev VM, Boltasseva A (2015) Nanoparticle plasmonics: going practical with transition metal nitrides. Materials Today 18(4):227–237
26. Habib A, Florio F, Sundararaman R (2018) Hot carrier dynamics in plasmonic transition metal nitrides. Journal of Optics 20(6):064001
27. Cortie MB, Giddings J, Dowd A (2010) Optical properties and plasmon resonances of titanium nitride nanostructures. Nanotechnology 21(11):115201
28. Ishii S, Shinde SL, Sugavaneshwar RP, Kaur M, Nagao T (2018) Harvesting sunlight with titanium nitride nanostructures. In: 2018 Progress in Electromagnetics Research Symposium (PIERS-Toyama), 1-4 Aug. pp 1286-1289
29. Guler U, Naik GV, Boltasseva A, Shalaev VM, Kildishev AV (2012) Performance analysis of nitride alternative plasmonic materials for localized surface plasmon applications. Applied Physics B 107(2):285–291
30. Guler U, Ndukaife JC, Naik GV, Nnanna AGA, Kildishev AV, Shalaev VM, Boltasseva A (2013) Local heating with lithographically fabricated plasmonic titanium nitride nanoparticles. Nano Letters 13(12):6078–6083
31. Naik GV, Schroeder JL, Ni X, Kildishev AV, Sands TD, Boltasseva A (2012) Titanium nitride as a plasmonic material for visible and near-infrared wavelengths. Opt Mater Express 2(4):478–489
32. Wang J, Zhang W, Zhu M, Yi K, Shao J (2015) Broadband perfect absorber with titanium nitride nano-disk array. Plasmonics 10(6):1473–1478
33. Gao H, Peng W, Liang Y, Chu S, Yu L, Liu Z, Zhang Y (2019) Plasmonic broadband perfect absorber for visible light solar cells application. Plasmonics 15:573–580
34. Ishii S, Shinde SL, Jevasuwan W, Fukata N, Nagao T (2016) Hot electron excitation from titanium nitride using visible light. ACS Photonics 3(9):1552–1557
35. Kamakura R, Murai S, Ishii S, Nagao T, Fujita K, Tanaka K (2017) Plasmonic–photonic hybrid modes excited on a titanium nitride nanoparticle array in the visible region. ACS Photonics 4(4):815–822
36. Podder S, Pal AR (2019) Plasmonic visible-NIR photodetector based on hot electrons extracted from nanostructured titanium nitride. Journal of Applied Physics 126(8):083108
37. Liang Q, Fu Y, Xia X, Wang L, Gao R (2018) Titanium nitride nano-disk arrays-based metasurface as a perfect absorber in the visible range. Modern Physics Letters B 32(01):1750365
38. Gao H, Peng W, Cui W, Chu S, Yu L, Yang X (2019) Ultraviolet to near infrared titanium nitride broadband plasmonic absorber. Optical Materials 97:109377

39. Juneja S, Shishodia MS (2019) Surface plasmon amplification in refractory transition metal nitrides based nanoparticle dimers. Optics Communications 433:89–96
40. Palik ED (1985) Handbook of optical constants of solids. Academic Press, Orlando
41. Haynes WM (2014) CRC handbook of chemistry and physics. CRC press
42. Gonçalves PAD, Xiao S, Peres NMR, Mortensen NA (2017) Hybridized plasmons in 2D nanoslits: from graphene to anisotropic 2D materials. ACS Photonics 4(12):3045–3054
43. Nikitin AY, Low T, Martin-Moreno L (2014) Anomalous reflection phase of graphene plasmons and its influence on resonators. Physical Review B 90(4):041407
44. Liu Z, Aydin K (2016) Localized surface plasmons in nanostructured monolayer black phosphorus. Nano Letters 16(6):3457–3462
45. Li M, Shen H, Zhuang L, Chen D, Liang X (2014) $SiO_2$ antireflection coatings fabricated by electron-beam evaporation for black monocrystalline silicon solar cells. International Journal of Photoenergy 2014:1–5
46. Fang C, Liu Y, Han G, Shao Y, Zhang J, Hao Y (2018) Localized plasmon resonances for black phosphorus bowtie nanoantennas at terahertz frequencies. Opt Express 26(21):27683–27693
47. Meng Y-L, Tan J, Xu K, Chen J, Jin G-J, Sun Y, Wang L-L, Zuo Z, Qin H-Y, Zhao Y, Guo J (2019) Salisbury screen optical color filter with ultra-thin titanium nitride film. Appl Opt 58(24):6700–6705
48. Ahangarani S, Sabour Rouhaghadam AR, Azadi M (2016) A review on titanium nitride and titanium carbide single and multilayer coatings deposited by plasma assisted chemical vapor deposition. Int J Eng Technol 29(5):677–687